

Double L_3M ionization of Pd induced by impact with medium-energy electronsW. Cao,^{1,*} J.-Cl. Dousse,¹ J. Hozszowska,¹ M. Kavčič,² Y. Kayser,¹ J.-L. Schenker,¹ and M. Žitnik²¹*Department of Physics, University of Fribourg, Ch. du Musée 3, CH-1700 Fribourg, Switzerland*²*J. Stefan Institute, P. O. Box 3000, SI-1001 Ljubljana, Slovenia*

(Received 16 September 2010; published 14 February 2011)

The electron-induced L_3M two-step double ionization cross sections of metallic Pd were determined experimentally for incident electron beam energies ranging from the double ionization threshold up to 18 keV. The double L_3M ionization cross sections were derived from the intensity ratios ($I_{L\alpha M}:I_{L\alpha}$) of the resolved M satellites to the parent diagram lines. The sample was bombarded with monoenergetic electrons from an energy-tunable 20-kV electron gun. The diagram and M -satellite x-ray lines were measured by means of high-resolution x-ray spectroscopy, using a reflection-type von Hamos bent crystal spectrometer. The two-step partial cross sections were determined by subtracting from the measured total double ionization cross sections the contributions due to the shake process and L_1 - $L_3M_{4,5}$ Coster-Kronig transitions. Despite the thick target employed in the present study, the dependence of the two-step cross sections on the incoming electron energy could be derived using a target slice decomposition method. It is shown that the obtained energy dependence can be well reproduced by the semiempirical parametrization model of Pattard and Rost.

DOI: [10.1103/PhysRevA.83.022708](https://doi.org/10.1103/PhysRevA.83.022708)

PACS number(s): 34.80.Dp, 32.30.Rj, 02.60.-x

I. INTRODUCTION

The electron-induced double ionization (DI) of neutral atoms may result from direct mechanisms for the ejection of two electrons without any internal atomic rearrangement or indirect mechanisms in which the ejection of a single inner-shell electron is followed by an Auger decay. Direct mechanisms can be subdivided into shake [1] and so-called two-step-one (TS1) and two-step-two (TS2) processes [2]. Shake results from the sudden change in the atomic potential as a consequence of an inner-shell ionization or nuclear decay, whereas the TS1 process describes the knock-out of a second bound electron by the first ionized electron and the TS2 process corresponds to the knock-out of two electrons from the same atom by a single incoming electron.

Two-step processes are important because they result from electron-electron interactions and therefore permit to investigate electron correlation effects. A straightforward method to study the TS processes is provided by ($e,3e$) experiments [3–5]. An alternative experimental approach consists to observe by means of high-resolution spectroscopy the radiative decay of atoms doubly ionized by electron impact. The latter method was used, for instance, by Mauron and Dousse [6]. In this study the double KL ionization induced in several light atoms by low-energy electrons was determined as a function of the incident electron energy. The energy-dependent double ionization cross sections (DICs) were derived from the measured intensity ratios $I_{K\alpha L^{(1)}}:I_{K\alpha L^{(0)}}$ of the resolved L -satellite-to-parent-diagram x-ray lines, using available experimental values for the electron-induced single K -shell ionization cross sections.

The determination of two-step L_3M DICs of mid- Z elements by means of the second experimental approach is, however, quite challenging for the following reasons. First, experimental data for the L -subshell electron-induced

single-ionization cross sections (EIICs) are scarce and suffer large uncertainties [7]. Many theoretical predictions for the EIICs are also questionable. For instance, those from Refs. [8] and [9] are in good overall agreement with the recent experimental values of Ref. [10], but they poorly reproduce the experimentally observed energy dependencies of the cross sections, especially for energies close to the ionization thresholds [10]. Second, the use of the satellite-to-diagram line ratio method requires that the M -satellite lines are well resolved from their parent diagram lines, which is not an easy task. According to multiconfiguration Dirac-Fock (MCDF) calculations [11,12], for mid heavy elements the average energy shift of the $L\alpha M$ satellites with respect to the parent $L\alpha$ diagram line is indeed only ~ 10 eV. Low-resolution detectors are unable to resolve such close lying satellite lines and the use of crystal spectrometers is thus mandatory. However, the latter suffer from a poor efficiency as compared to low-resolution detectors, which makes the measurements more difficult and time-consuming. Last but not least, $L_{1,2}$ - L_3M Coster-Kronig (CK) transitions, if energetically allowed, contribute significantly to the observed L_3M double ionization and the measured $L\alpha M$ to $L\alpha_{1,2}$ intensity ratios have to be corrected to account for this indirect DI contribution. Therefore, for the determination of the TS cross sections via the satellite-to-diagram line intensity ratio method, reliable CK probabilities are needed.

Analytical expressions for the EIICs based on the distorted-wave Born approximation (DWBA) [13] were published recently [14]. The theoretical values obtained from these analytical expressions were found to be in good agreement with the experimental cross sections reported for the L subshells in Ref. [15] and to provide reliable results even for energies close to the ionization thresholds. On the other hand, a precise value was obtained lately for the L_1 - $L_3M_{4,5}$ CK yield of Pd by means of synchrotron-radiation-based high-resolution x-ray spectroscopy [16]. Hence Pd was chosen in the present work to investigate the contribution of TS processes to the electron-induced L_3M double ionization of mid- Z elements.

*wei.cao@unifr.ch

II. EXPERIMENT

The experiment was performed at the Physics Department of the University of Fribourg, employing a high-resolution reflecting-type von Hamos curved crystal spectrometer [17] for the measurements of the target x-ray emission. The sample fluorescence was produced by bombarding the Pd target with the beam from an energy-tunable thermoionic electron gun. The latter was equipped with a Ta disk cathode and electrostatic focusing and deflection electrodes. With this cathode, the electron gun can be operated safely at a pressure of 10^{-6} mbar which corresponds to the vacuum in the spectrometer chamber for standard operation. The accelerating voltage can be varied from 50 V to 20 kV, with a precision of 1 V. The beam current is independently adjustable from 1 μ A to 1 mA. Thanks to a feedback stabilized emission current control, the relative stability of the electron beam intensity is better than 0.1%.

A top view of the experimental setup is depicted in Fig. 1. As shown, the electron beam was perpendicular to the crystal and detector translation axes which are both parallel to the dispersion direction of the spectrometer. The Pd target consisted of a thick metallic foil. It was positioned so that the angle δ between the normal to the foil and the beam direction was 29.6° . The exit angle of the x rays relatively to the normal to the sample surface was thus $\kappa = \pi/2 - \delta - \theta$, where θ stands for the Bragg angle. To avoid that the foil melts as a result of the heatload due to the electron bombardment, a rather large thickness of 114 μ m was chosen. The von Hamos spectrometer was operated in the so-called slit geometry. In this geometry, the target is viewed by the crystal through a narrow slit which is located on the translation axis of the detector and serves as the effective source of x-ray radiation. For this experiment, a slit width of 0.2 mm was adopted as the best compromise between a high-enough energy resolution and an acceptable spectrometer luminosity. Furthermore, to reduce the background a cylindrical collimator was installed between the electron gun and the target and the spectrometer slit was covered with a ~ 20 - μ m-thick Be window. The fluorescence x rays from the target were diffracted in first order by a 10-cm-high \times 5-cm-long \times 0.15-mm-thick quartz ($1\bar{1}0$) crystal plate bent cylindrically to a radius of 25.4 cm. The diffracted x rays were recorded by a thermoelectrically cooled (-40°C) back

illuminated charge-coupled device (CCD) camera consisting of 1340×400 pixels with pixel sizes of $20 \times 20 \mu\text{m}^2$.

The $L\alpha$ x-ray emission spectrum of Pd was recorded for 15 different electron beam energies ranging from 4 to 18 keV (nominal energies). Depending on the incident electron energy and beam current, the collecting times varied between 1 and 5 h. To probe the effect of L_3M vacancy states with more than one hole in the M shell (see the Appendix), measurements of the $L\beta_1$ (L_2 - M_4 transition) and $L\beta_{3,4}$ (L_1 - $M_{3,2}$ transitions) x-ray lines were also performed. The $L\beta_1$ line was measured at two electron beam energies ($E_e = 10$ keV and 15 keV), while the $L\beta_{3,4}$ lines were measured at a single beam energy ($E_e = 16$ keV). For the energy calibration of the $L\alpha_{1,2}$ x-ray spectra, the $K\alpha_1$ lines of Cr and Mn were measured with the same crystal but in second order of diffraction, using the reference energies of 5414.805(7) eV and 5898.801(8) eV reported in Ref. [18]. The same method was employed to calibrate in energy the $L\beta_1$ and $L\beta_{3,4}$ spectra, but in this case, the $K\alpha_1$ x-ray lines of Mn and Fe ($E = 6404.006(10)$ eV [18]) were used as reference energies.

III. DATA ANALYSIS AND METHODOLOGY

This section is subdivided into three parts. In the first, the procedure employed to fit the measured $L\alpha$ x-ray spectra and in particular the M -satellite structures is described. Since the fitted intensities of the M satellites are due not only to the TS mechanism of interest but also to the shake and CK processes, the methods used to determine and subtract the shake and CK contributions from the observed satellite-to-diagram line intensity ratios are first presented. Subsequently, it is shown how the TS cross sections can be derived from the intensity ratios corresponding to the sole TS process and how the variation of these cross sections as a function of the incoming electron energy can be determined using two different theoretical models for the energy dependence. In the third part, a different method which is based on the decomposition of the sample into slices of different thicknesses and permits to determine the energy dependence of the TS cross sections without resorting to any theoretical model is presented.

A. Spectra fitting

For the Bragg angle region corresponding to the $L\alpha$ x-ray spectrum, the energy resolution of the von Hamos spectrometer was about 1.1 eV. This resolving power of $\sim 4 \times 10^{-4}$ allowed us to resolve the $L\alpha_{1,2}$ doublet and to separate the latter from its M -shell satellite structure. On the contrary, the N -shell satellites could not be resolved because, as shown by MCDF calculations [19], they are fully overlapping with the $L\alpha_{1,2}$ diagram lines, which leads to a nonlifetime broadening of the latter. The $L\alpha_{1,2}$ diagram lines and the unresolved $L\alpha N$ satellite lines were fitted with two Lorentzians, while a single Lorentzian was employed to fit the bump corresponding to the M -satellite structure. For illustration, the fitted $L\alpha_{1,2}$ spectrum measured at an incident electron beam energy of 8 keV is depicted in Fig. 2. The M -satellite region is shown enlarged in the inset for three other beam energies (4, 5, and 18 keV). The energies and relative intensities of the individual MCDF

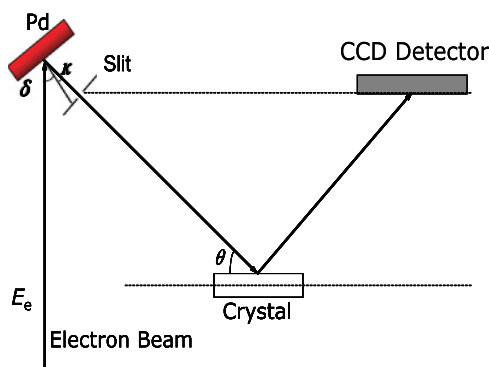


FIG. 1. (Color online) Top view of the experimental setup. The dotted lines represent the translation axes along which the crystal and CCD detector can be moved to change the central Bragg angle (for further details see Ref. [17]).

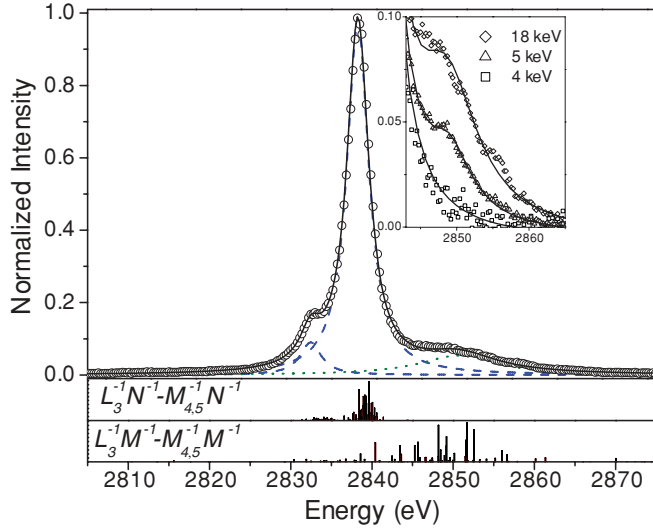


FIG. 2. (Color online) Fitted high-resolution $L\alpha$ x-ray spectrum of Pd at the incident electron beam energy of 8 keV. The solid thick line stands for the total fit to the experimental data (open circles), while the dashed lines and the dotted line represent the $L\alpha_{1,2}$ diagram and $L\alpha M$ satellite lines, respectively. The stick spectra in the lower panels correspond to the results of the MCDF calculations for the $L\alpha N$ and $L\alpha M$ satellite transitions. In the inset, the evolution of the M satellites as a function of the beam energy is shown.

multiplet components corresponding to the $L\alpha N$ and $L\alpha M$ satellite transitions are also shown in the bottom panels.

For the spectra induced by the lower-energy electrons, the $L\alpha M$ satellites are weak and the fluctuations of the experimental points rather large so the fit of the satellite structure with a single Lorentzian looks quite reasonable. At higher electron energies, however, the intensity of the M -shell satellites increases and some fine structures can be observed (see inset of Fig. 2). In this case the shape of the M -satellite region is more difficult to reproduce with a single Lorentzian. To probe the goodness of the satellite intensities returned by the single Lorentzian fits, the $L\alpha$ spectrum measured at 12 keV was refitted, using two Lorentzians for the diagram lines as before but four Lorentzians for the M satellites. All

parameters were let free in the fit. The spectrum measured at 12 keV was chosen as probe spectrum because at this energy the $L\alpha M$ to $L\alpha$ intensity ratio was found to be the biggest. The result of the new analysis is presented in Fig. 3. As shown, the fit is of good quality. In particular, the shape of the $L\alpha M$ satellite region is well reproduced by the four Lorentzians. However, it can be noted that some components on the left side of the MCDF stick spectrum coincide in position with the $L\alpha_1$ Lorentzian and, to a smaller extent, with the $L\alpha_2$ one, but clearly not with the four Lorentzians used to fit the satellite region. The fitted intensity of the diagram lines is therefore too big and the one of the satellites too small. To account for this impreciseness of the analysis, the satellite-to-diagram intensity ratio was corrected as follows:

$$i_{\text{cor}} = i_{\text{fit}} \frac{1 + \sum \frac{I_{\text{MCDF}}^{\text{out}}}{I_{\text{MCDF}}^{\text{in}}}}{1 - i_{\text{fit}} \frac{\sum I_{\text{MCDF}}^{\text{out}}}{\sum I_{\text{MCDF}}^{\text{in}}}}, \quad (1)$$

where $\sum I_{\text{MCDF}}^{\text{in}}$ represents the sum of the relative intensities of the MCDF components covered by the profile corresponding to the sum of the four satellite Lorentzians and $\sum I_{\text{MCDF}}^{\text{out}}$ the sum of the relative intensities of the MCDF components lying outside this profile. Using the above formula, a value $i_{\text{cor}} = 0.204(5)$ was found for the corrected $L\alpha M$ -to- $L\alpha$ intensity ratio, whereas the uncorrected ratio provided by the new fit was $i_{\text{fit}} = 0.156(4)$. It is somewhat surprising to note that the corrected ratio is in very good agreement with the ratio of 0.201(8) obtained with the single Lorentzian fit. This is probably due to the fact that the low-energy tail of the broad single Lorentzian is partly overlapping with the diagram lines and covers thus the MCDF components that are lying outside the sum profile in the four-Lorentzians fit. Finally, as the ratios obtained by the two methods were consistent, we decided to use the simplest method, i.e., to fit the satellite region of the 15 measured spectra with a single Lorentzian.

B. Parametrizations

For the beam energy E_e the corrected experimental intensity ratio $I_{L\alpha M}$ to $I_{L\alpha_{1,2}}$ can be written as:

$$i_{\text{cor}}(E_e) = \frac{\omega_{L\alpha M}}{\omega_{L\alpha}} \frac{\Omega^* c^* [N_{\text{shake}}(E_e) + f_{13}^{LLM} N_{L_1}(E_e) + N_{\text{TS}}(E_e)]}{\Omega c [N_{L_3}(E_e) - N_{\text{shake}}(E_e) + (f_{13}^{LLN} + f_{12} f_{23} + f'_{13}) N_{L_1}(E_e) + f_{23} N_{L_2}(E_e)]}, \quad (2)$$

where $\omega_{L\alpha}$ and $\omega_{L\alpha M}$ denote the $L\alpha_{1,2}$ and $L\alpha M$ partial x-ray fluorescence yields. The $\omega_{L\alpha M}$ -to- $\omega_{L\alpha}$ ratio can be deduced from a statistical scaling procedure [16,20]. The instrumental efficiency is given by the term Ωc for the diagram lines and $\Omega^* c^*$ for the M satellites, where Ω , respectively Ω^* , is the solid angle of the spectrometer and c , respectively c^* , an instrumental constant which takes into consideration the crystal reflectivity and CCD detector efficiency. As the energy difference between the diagram and satellite lines is only about 10 eV, the ratio $\frac{\Omega^* c^*}{\Omega c}$ is nearly equal to 1. The coefficients f_{ij} ($1 \leq i < j \leq 3$) represent the L_i - L_j subshell CK yields; f_{13}^{LLM} and f_{13}^{LLN} the partial CK yields of the L_1 - $L_3 M_{4,5}$

and L_1 - $L_3 N$ transitions, respectively; and f'_{13} the L_1 to L_3 hole-transfer rate resulting from the L_1 - L_3 radiative transition. However, the value of f'_{13} is very small as compared to the CK yields [21] and can thus be neglected.

The symbols N_s represent the number of atoms that undergo per second a given process s . Taking the target self-absorption into consideration, $N_s(E_e)$ can be written as:

$$N_{L_i, \text{shake, TS}}(E_e) = \frac{N_A N_e \rho}{A} \int_0^{h_{L_i, \text{shake, TS}}} \sigma_{L_i, \text{shake, TS}}(E(x)) \times \exp\left[-\mu \frac{x}{\cos(\kappa)}\right] dx. \quad (3)$$

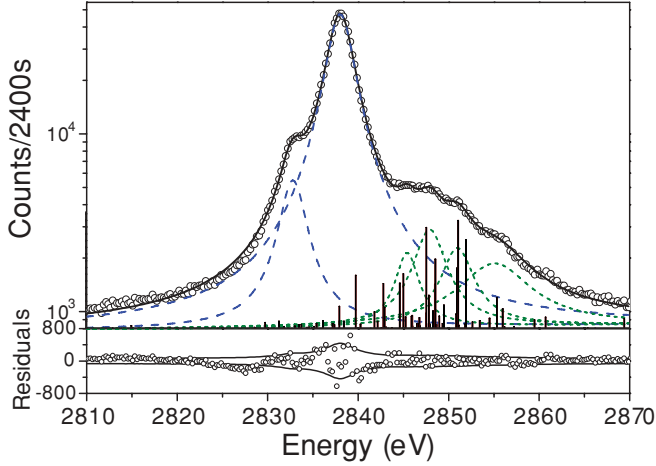


FIG. 3. (Color online) Pd high-resolution $L\alpha$ x-ray spectrum induced by the 12-keV electron beam and fitted with six Lorentz functions. The solid thick line represents the total fit to the experimental data (open circles), the dashed lines the fitted $L\alpha_{1,2}$ diagram transitions, the dot lines the fitted $L\alpha M$ satellites and the stick spectrum the results of the MCDF calculations for the $L\alpha M$ satellites. Fit residuals are shown in the lower panel where they are compared with the statistical errors ($\pm 2\sigma$) of the data points (thin lines).

Here N_A is the Avogadro constant, N_e the number of electrons impinging per second on the target, ρ the density of the sample, and A its atomic mass number. In the integral, $\sigma_{L_i, \text{shake, TS}}(E)$ stands for the single ionization cross section of the L_i subshell, the shakeoff cross section, or the cross section of the TS process; μ is the total absorption coefficient at the energy of the emitted $L\alpha$ or $L\alpha M$ x ray; and κ is the above-mentioned x-ray exit angle.

Due to the lack of experimental EIICSs for the Pd L subshells, the formula proposed by Campos *et al.* in Ref. [14] was used:

$$\sigma_{L_i}(U) = \frac{A_{L_i}}{B_{L_i} + U} \ln(U), \quad (4)$$

where the dimensionless parameter $U = E/E_{L_i}^{\text{thr}}$ denotes the overvoltage of the incoming electron, E is the electron energy, and $E_{L_i}^{\text{thr}}$ the ionization threshold energy for the L_i subshell. The parameters A_{L_i} and B_{L_i} depend on the atomic number Z of the target. They can be derived from the equations given in Ref. [14].

The shakeoff cross section σ_{shake} was obtained by multiplying the single ionization cross section σ_{L_3} by the shake probability given by the Thomas model [22]:

$$P_{\text{Thomas}}(E) = P_{\infty} \exp \left[-\frac{r^2 E_s^2}{15.32(E - E_{\text{shake}}^{\text{thr}})} \right]. \quad (5)$$

In the above equation, E_s is the shake energy, r the distance covered by the ionized electron during the time the atomic potential changes and P_{∞} the shake probability at the saturation. The energies E , E_s , and $E_{\text{shake}}^{\text{thr}}$ are in eV and the radius r in Å. For E_s , the average binding energy of the M -shell electrons in Ag ($Z = 47$) was employed [($Z + 1$)-potential approximation]. The theoretical $L_3 M$ shakeoff threshold was

assumed to be the same as the one of the $L_3 M$ TS threshold:

$$E_{\text{shake}}^{\text{thr}} = E_{TS}^{\text{thr}} = E_{L_3}^{\text{thr}} + E_s. \quad (6)$$

As suggested in Ref. [23], the distance r was approximated to the average value of the radii for which the squared $3d$ wave functions peak in ionic Pd^+ . $3d$ orbitals were chosen because of their bigger shake probability and larger electron population as compared to $3s$ and $3p$ orbitals. The value of P_{∞} was calculated in the framework of the sudden approximation model [24] using self-consistent Dirac-Fock wave functions from the code of Ref. [25]. It should be mentioned here that the Thomas model was originally developed for shake processes following photoionization. We have thus implicitly assumed that the shake probability is independent from the first ionization mechanism. This assumption is, however, not critical because the shake contribution to the total $L_3 M$ DI was found to be small with respect to other processes (see Sec. IV).

The upper integration limits $h_{L_i, \text{shake, TS}}$ in Eq. (3) correspond to the depths in the sample at which the electron energy $E(x) = E_{L_i, \text{shake, TS}}^{\text{thr}}$, where $E_{L_i, \text{shake, TS}}^{\text{thr}}$ is the threshold energy of the single L_i subshell ionization, shake or TS process. Providing that the multiple scattering of the incoming electrons can be neglected, these depths can be derived from the stopping power $s(E)$:

$$\begin{aligned} s(E) &= -\frac{dE}{dx / \cos \delta} \rightarrow h_{L_i, \text{shake, TS}} = x|_0^{h_{L_i, \text{shake, TS}}} \\ &= -\int_{E_e}^{E_{L_i, \text{shake, TS}}^{\text{thr}}} \frac{\cos \delta}{s(E)} dE, \end{aligned} \quad (7)$$

where δ is the angle between the incoming electron beam and the normal to the sample surface. As the coordinate x is equal to zero at the front surface of the sample, the above

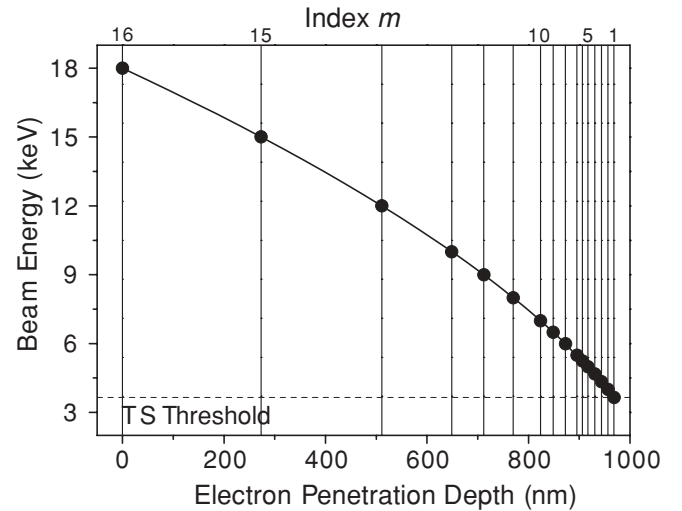


FIG. 4. Target slices and effective TS target thicknesses for the employed electron beam energies. The highest beam energy (18 keV) corresponds to the index $m = 16$, the lowest one (4 keV) to the index $m = 2$, whereas the index $m = 1$ is assigned to the threshold energy for the TS process. The effective thickness corresponding to a particular beam energy $E_e^{(m)}$ is given by the difference between the x coordinates of the vertical lines labeled 1 and m . Similarly, the thickness of the m -th slice is given by the difference between the x coordinates of the vertical lines labeled m and $m+1$.

depths can be interpreted as effective sample thicknesses for the three processes. The values of $s(E)$ were determined by interpolating the data quoted in the NIST tables [26] with the program ESTAR [27], using a grid of 10-eV steps. A trapezoidal integration algorithm was then employed to calculate numerically the effective sample thicknesses for the different beam energies.

As the constant $C = \frac{N_A N_e \rho}{A}$ in Eq. (3) can be set as a common factor in both the numerator and denominator of Eq. (2) and thus cancels out, the following new parameters will be used in further discussions:

$$\Pi_{L_i, \text{shake, TS}}(E_e) = N_{L_i, \text{shake, TS}}(E_e)/C. \quad (8)$$

The quantities $\Pi_{L_i, \text{shake, TS}}(E_e)$, named hereafter *cross-section integrals*, have the dimension of a cross section multiplied by a length. Replacing $N_{L_i, \text{shake, TS}}(E_e)$ by the corresponding cross-section integrals, one can write Eq. (2) in the following form:

$$i_{\text{cor}}(E_e) = i_{\text{shake}}(E_e) + i_{\text{CK}}(E_e) + i_{\text{TS}}(E_e), \quad (9)$$

where the partial ratios corresponding to the shake, Coster-Kronig and two-step processes are given by:

$$i_{\text{shake}}(E_e) = \frac{\omega_{L\alpha M}}{\omega_{L\alpha}} \frac{\Pi_{\text{shake}}(E_e)}{D(E_e)}, \quad (10)$$

$$i_{\text{CK}}(E_e) = \frac{\omega_{L\alpha M}}{\omega_{L\alpha}} \frac{f_{13}^{LLM} \Pi_{L_1}(E_e)}{D(E_e)}, \quad (11)$$

$$i_{\text{TS}}(E_e) = \frac{\omega_{L\alpha M}}{\omega_{L\alpha}} \frac{\Pi_{\text{TS}}(E_e)}{D(E_e)}. \quad (12)$$

In the three above equations, the function $D(E_e)$ is defined by:

$$D(E_e) = \Pi_{L_3}(E_e) - \Pi_{\text{shake}}(E_e) + (f_{13}^{LLN} + f_{12}f_{23})\Pi_{L_1}(E_e) + f_{23}\Pi_{L_2}(E_e). \quad (13)$$

The experimental TS cross-section integrals can then be deduced from Eqs. (12) and (9):

$$\Pi_{\text{TS}}^{\text{expt}}(E_e) = \frac{\omega_{L\alpha}}{\omega_{L\alpha M}} D(E_e) [i_{\text{cor}}(E_e) - i_{\text{shake}}(E_e) - i_{\text{CK}}(E_e)]. \quad (14)$$

To determine the TS cross section or TS cross-section integral at any electron energy E , an analytical expression is, however, needed. Two different approaches were employed. In the first one, an energy dependence similar to the one proposed by Campos [14] was used:

$$\sigma_{\text{TS}}(U') = \frac{A_{\text{TS}}}{B_{\text{TS}} + U'} \ln(U'). \quad (15)$$

In the above equation the unknown parameters are A_{TS} and B_{TS} , the threshold energy being given by Eq. (6). The notation U' is employed to distinguish the TS overvoltage from the single ionization overvoltage U occurring in Eq. (4).

As the Campos model is usually employed for the determination of single ionization cross sections, an alternative approach based on the model of Pattard and Rost [28,29] was also probed. In this model the electron-induced multi-ionization cross section has the following form:

$$\sigma(E) = \sigma_M \left[\frac{E - E_{\text{thr}}}{E_M - E_{\text{thr}}} \right]^\alpha \left[\frac{\alpha + 1}{\alpha \left(\frac{E - E_{\text{thr}}}{E_M - E_{\text{thr}}} \right) + 1} \right]^{(\alpha+1)}, \quad (16)$$

where E_M and σ_M are the energy and amplitude of the maximum cross section. For the threshold exponent α , a value of 2.2704 was adopted as suggested in Ref. [29] for mid heavy and heavy elements.

To determine the values of the parameters A_{TS} and B_{TS} of Eq. (15) and σ_M and E_M of Eq. (16) that reproduce at best the experimental data, the least-squares fit from the MATLAB optimization package was employed. The algorithm is based on the trust-region reflective Newton method [30]. Briefly speaking, the program minimizes the sum S defined by:

$$S = \sum \frac{[\Pi_{\text{TS}}^{\text{fit}}(E_e) - \Pi_{\text{TS}}^{\text{expt}}(E_e)]^2}{\sigma^2(E_e)}, \quad (17)$$

where $\Pi_{\text{TS}}^{\text{fit}}(E_e)$ and $\Pi_{\text{TS}}^{\text{expt}}(E_e)$ stand for the fitted and experimental values of the two-step cross-section integrals and $\sigma(E_e)$ are the uncertainties of the experimental values. The goodness of the numerical optimizations performed with the Campos and Pattard-Rost models was probed by calculating the reduced chi-squares χ_r^2 of the corresponding fits. Note that the reduced chi-square χ_r^2 corresponds to the chi-square χ^2 [i.e., the minimum value of the function S defined in Eq. (17)] divided by the degree of freedom $\nu = N - n - 1$, where N is the number of data points and n the number of fitting parameters.

C. Experimental determination of the TS cross sections as a function of the electron energy

As shown by Eq. (3) the calculation of the cross sections $\sigma_{\text{TS}}(E)$ requires the knowledge of the function $E(x)$. In principle, the variation $E(x)$ of the electron energy as a function of the penetration depth could be parametrized using a power law for the energy dependence and determining the constants entering the power law equation with the known stopping powers $s(E)$. In this work, another approach was employed. First, the different beam energies were numbered from 2 for the lowest beam energy to 16 for the highest one, the number 1 being assigned to the threshold energy of the TS process [i.e., $E_e^{(1)} = E_{\text{TS}}^{\text{thr}}$, $E_e^{(2)} = 4$ keV, ..., $E_e^{(16)} = 18$ keV]. The thick target was then divided in several slices of variable thicknesses, the thickness of the slice number i ($i = 1, 2, \dots, 15$) being given by $h_{\text{TS}}^{(i+1)} - h_{\text{TS}}^{(i)}$, where $h_{\text{TS}}^{(i)}$ represents the effective thickness of the target for the i -th beam energy. For $i > 1$, the effective thicknesses were calculated with Eq. (7), whereas $h_{\text{TS}}^{(1)} = 0$ per definition.

The decomposition of the thick target into slices is depicted in Fig. 4. The y coordinates of the black points correspond to the nominal beam energies. As shown, the curve passing through these points has a negative curvature, which indicates that the specific energy losses of the electrons grow with decreasing energies. The slice number is given by the index m associated to the right boundary of the slice. The virtual front surface for electron beam impact with a nominal energy of $E_e^{(m)}$ is defined by the left boundary of the $(m - 1)$ -th slice. The thickest slice is the 15th one which is related to the beam energy $E_e^{(16)} = 18$ keV. Its thickness which corresponds to an energy loss of 3 keV is 273 nm. For this beam energy, the effective target thickness is 969 nm. For comparison, for the next lower energy

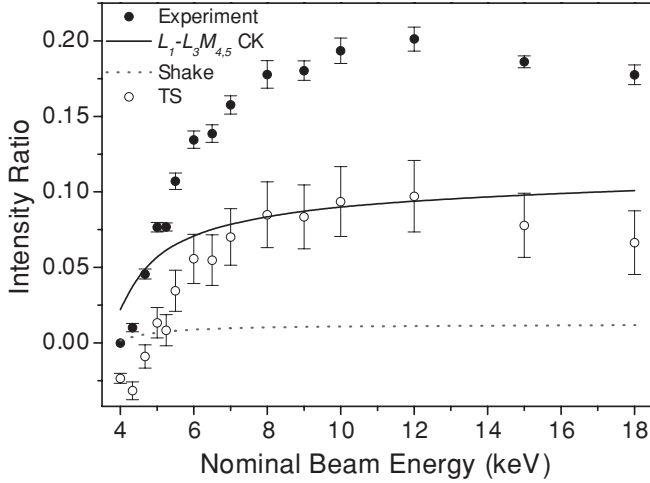


FIG. 5. Experimental $L\alpha M$ -to- $L\alpha_{1,2}$ intensity ratios (full circles) as a function of the nominal electron beam energy. The partial ratios corresponding to the L_1 - $L_3M_{4,5}$ Coster-Kronig (solid line), shakeoff (dashed line), and two-step (open circles) processes are also shown.

beams $E_e^{(15)} = 15$ keV, $E_e^{(14)} = 12$ keV, and $E_e^{(13)} = 10$ keV, the effective thicknesses are 696, 458, and 320 nm, respectively.

According to Eqs. (3) and (8), the experimental cross-section integrals $\Pi_{\text{TS}}[E_e^{(m)}]$ can then be expressed as:

$$\Pi_{\text{TS}}^{\text{expt}}[E_e^{(m)}] = \sum_{i=2}^m \int_{h_{\text{TS}}^{(i-1)}}^{h_{\text{TS}}^{(i)}} \sigma_{\text{TS}}(E(x)) \exp\left[-\mu \frac{x}{\cos(\kappa)}\right] dx. \quad (18)$$

Using a trapezoidal algorithm to evaluate the integrals in Eq. (18), the cross-section integrals can be written as follows:

$$\begin{aligned} \Pi_{\text{TS}}^{\text{expt}}(E_e^m) &\approx \sum_{i=2}^m [h_{\text{TS}}^{(i)} - h_{\text{TS}}^{(i-1)}] \frac{\sigma_{\text{TS}}[E_e^{(i)}] + \sigma_{\text{TS}}[E_e^{(i-1)}]}{2} \\ &\times \exp\left[-\mu \frac{h_{\text{TS}}^{(m)} - h_{\text{TS}}^{(i)}}{\cos(\kappa)}\right] \\ &\times \exp\left[-\mu \frac{h_{\text{TS}}^{(i)} - h_{\text{TS}}^{(i-1)}}{2 \cos(\kappa)}\right]. \end{aligned} \quad (19)$$

The terms $\exp[-\mu \frac{h_{\text{TS}}^{(i)} - h_{\text{TS}}^{(i-1)}}{2 \cos(\kappa)}]$ and $\exp[-\mu \frac{h_{\text{TS}}^{(m)} - h_{\text{TS}}^{(i)}}{\cos(\kappa)}]$ in Eq. (19) account for the absorption of the emitted x rays in the target layer extending from the middle of the $(i-1)$ -th slice to the virtual front surface. From Eq. (19) the following recurrence relation between the cross-section integrals $\Pi_{\text{TS}}^{\text{expt}}[E_e^{(m)}]$ and $\Pi_{\text{TS}}^{\text{expt}}[E_e^{(m-1)}]$ can be derived:

$$\begin{aligned} \Pi_{\text{TS}}^{\text{expt}}[E_e^{(m)}] &= \Pi_{\text{TS}}^{\text{expt}}[E_e^{(m-1)}] \exp\left[-\mu \frac{h_{\text{TS}}^{(m)} - h_{\text{TS}}^{(m-1)}}{\cos(\kappa)}\right] \\ &+ \frac{\sigma_{\text{TS}}[E_e^{(m)}] + \sigma_{\text{TS}}[E_e^{(m-1)}]}{2} [h_{\text{TS}}^{(m)} - h_{\text{TS}}^{(m-1)}] \\ &\times \exp\left[-\mu \frac{h_{\text{TS}}^{(m)} - h_{\text{TS}}^{(m-1)}}{2 \cos(\kappa)}\right]. \end{aligned} \quad (20)$$

Finally, using the approximation

$$\frac{\sigma_{\text{TS}}[E_e^{(m)}] + \sigma_{\text{TS}}[E_e^{(m-1)}]}{2} = \sigma_{\text{TS}}(E_{\text{av}}), \quad (21)$$

where $E_{\text{av}} = \frac{E_e^{(m)} + E_e^{(m-1)}}{2}$, the TS cross section $\sigma_{\text{TS}}(E_{\text{av}})$ is given by:

$$\sigma_{\text{TS}}(E_{\text{av}}) \approx \frac{\Pi_{\text{TS}}^{\text{expt}}[E_e^{(m)}] - \Pi_{\text{TS}}^{\text{expt}}[E_e^{(m-1)}] \exp\left[-\mu \frac{h_{\text{TS}}^{(m)} - h_{\text{TS}}^{(m-1)}}{\cos(\kappa)}\right]}{[h_{\text{TS}}^{(m)} - h_{\text{TS}}^{(m-1)}] \exp\left[-\mu \frac{h_{\text{TS}}^{(m)} - h_{\text{TS}}^{(m-1)}}{2 \cos(\kappa)}\right]}. \quad (22)$$

It should be noted at this point that E_{av} represents the ‘‘average’’ energy of the $E_e^{(m)}$ electron beam in the $(m-1)$ -th slice and not the average energy with respect to the whole penetration depth.

IV. RESULTS AND DISCUSSION

As shown in the preceding section, a precise determination of the TS process contribution to the observed $L\alpha M$ to $L\alpha$ intensity ratios requires a reliable knowledge of the electron-induced single ionization cross sections σ_{L_i} . Therefore, the DWBA-based predictions from Eq. (4) were carefully probed by comparing them to experimental L x-ray production cross sections measured for neighboring elements [31]. The coefficients A_{L_i} and B_{L_i} of Eq. (4) were computed using the Z -dependence formula given in Ref. [14], whereas for the calculation of the overvoltages U , the experimental L_i -subshell ionization thresholds reported in Ref. [16] were used. The latter and the employed A_{L_i} and B_{L_i} values are listed in Table I. From the comparison it was found that the theoretical values from Eq. (4) are reliable over a wide range of incident electron energies. It should be mentioned, however, that the goodness of the theoretical predictions was more difficult to probe for impact energies just above the ionization thresholds because experimental data are scarce in these energy regions and affected by larger uncertainties due to the tiny values of the x-ray production cross sections, particularly those corresponding to the L_1 subshell. Nevertheless, relative uncertainties of 10% comparable to the experimental errors quoted in Ref. [31] for the total L -line x-ray production cross sections of neighboring elements were adopted for the present cross sections σ_{L_i} . The bremsstrahlung and scattering cross sections of medium-energy electrons are small as compared to the L_i EIICs [10,32] so they were neglected. The influence of the multiple M -shell ionization was also probed by performing complementary measurements of the $L\beta_1$ and $L\beta_{3,4}$ x-ray emission lines. As shown in the Appendix, the

TABLE I. Coster-Kronig yields f_{ij} , ionization threshold energies $E_{L_i}^{\text{thr}}$ and electron impact ionization cross section parameters A_{L_i} and B_{L_i} for the palladium L_i ($i = 1, 2, 3$) subshells. The $E_{L_i}^{\text{thr}}$ are expressed in keV, the A_{L_i} 's in kb, whereas the B_{L_i} 's are dimensionless parameters.

i	f_{i2}	f_{i3}^{LLM}	f_{i3}^{LLN}	$E_{L_i}^{\text{thr}}$	A_{L_i}	B_{L_i}
1	0.047(1)	0.406(23)	0.324(32)	3.61	7.047	0.27426
2	–	–	0.164(33)	3.32	10.305	0.08182
3	–	–	–	3.17	23.614	0.06025

effect of this multiple ionization is also negligibly small and was thus neither considered. The shakeoff cross sections were determined according to the method presented in Sec. III B and the CK rates f_{ij} were taken from Ref. [16] (see Table I). Note that for Pd $f_{23} = f_{23}^{LLN}$ because L_2 - L_3M CK transitions are energetically forbidden.

The experimental $L\alpha M$ to $L\alpha$ intensity ratios obtained in the present work are shown in Fig. 5 as a function of the nominal electron beam energy. The CK, shakeoff (SO), and two-step (TS) contributions to the intensity ratios are also depicted. They were computed using the method and the equations presented in Sec. III B. For the TS ratios, negative values were found for the lowest beam energies. This is probably due to the fact that the L_1 EIICSs calculated with Eq. (4) are somewhat overestimated in the energy region close to the L_1 ionization threshold. On the other hand, as shown in Fig. 5, for all beam energies the SO ratios were found to be small as compared to the ones of the two other processes. This is, however, not surprising since it is well known that the probability to observe a shakeoff process in the M shell as a result of a primary L -shell ionization is very small.

The experimental cross-section integrals Π_{TS}^{expt} determined from Eq. (14) are listed in the third column of Table II and also presented in Fig. 6 as a function of the nominal beam energies. The estimated errors stem mainly from the uncertainties of the Coster-Kronig yields (2–20%, see table I) and the relative uncertainties of 10% for the L -subshell cross sections σ_{L_i} . For the determination of the experimental threshold energy of the TS process, a method similar to the one used in Ref. [33] to deduce the Cu double K -shell ionization threshold was employed. The threshold energy was indeed determined by calculating the x coordinate of the intersection point of the linear regression lines defined by the data points corresponding

TABLE II. Nominal electron beam energies E_e in keV, experimental $L\alpha M$ to $L\alpha$ intensity ratios, cross-section integrals $\Pi_{TS}^{\text{expt}}(E_e)$ in kb nm, average beam energies E_{av} in keV, and cross sections $\sigma_{TS}(E_{\text{av}})$ in kb. E_{av} represents the average beam energy in the first slice crossed by the incoming electrons. The $I_{L\alpha M}/I_{L\alpha}$ uncertainties correspond to statistical errors from the least-squares fitting procedure.

E_e	$I_{L\alpha M}/I_{L\alpha}$	$\Pi_{TS}^{\text{expt}}(E_e)$	E_{av}	$\sigma_{TS}(E_{\text{av}})$
4.00	0	-1.6(0.2)	-	-
4.33	0.010(3)	-4.2(0.7)	-	-
4.67	0.046(3)	-1.9(1.7)	-	-
5.00	0.077(3)	4.1(3.1)	-	-
5.25	0.077(3)	3.2(4.0)	5.13	-0.08(47)
5.50	0.107(5)	16.1(6.3)	5.38	1.19(68)
6.00	0.135(6)	36.0(10.2)	5.75	0.89(53)
6.50	0.139(6)	46.4(13.8)	6.25	0.46(72)
7.00	0.156(6)	74.3(19.0)	6.75	1.15(94)
8.00	0.178(9)	128.7(31.5)	7.50	1.09(69)
9.00	0.180(6)	166.9(40.2)	8.50	0.77(88)
10.0	0.193(8)	233.7(54.6)	9.50	1.22(1.09)
12.0	0.201(8)	339.1(78.2)	11.0	0.98(70)
15.0	0.186(4)	380.4(99.7)	13.5	0.44(55)
18.0	0.178(6)	402.9(125.1)	16.5	0.38(60)

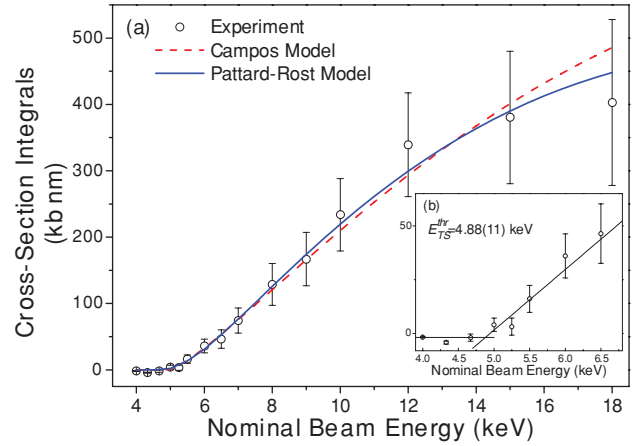


FIG. 6. (Color online) Two-step cross-section integrals vs. nominal electron beam energies. (a) Present experimental values (open circles) and results of the least-squares fits to the experimental data with Eq. (18) using the Pattard-Rost [28,29] (solid line) and Campos [14] (dashed line) models for the energy dependence of the cross sections. (b) Enlarged view of the low-energy and fast-increase regions showing the data points and regression lines employed to determine the threshold energy of the TS process.

to the three lowest beam energies, respectively the five data points lying in the region of fast increase [see Fig. 6(b)]. A value of 4.88 ± 0.11 keV was found. The uncertainty obtained for E_{TS}^{thr} is due to the statistical errors affecting the low-energy data and to the propagation of the errors related to the subtraction of the cross sections corresponding to the other processes. Note that a more precise determination of E_{TS}^{thr} would represent a challenging task because for electron energies close to the threshold the $L\alpha M$ satellite lines due to the TS process are characterized by very low count rates, which leads to high statistical errors. In addition, available experimental CK yields [16,34,35] all suffer from rather large uncertainties. On the other hand, the obtained threshold energy is bigger than the value of 3.65 keV provided by the $(Z+1)$ potential approximation [Eq. (6)]. This trend, however, is consistent with former observations, e.g., the one concerning the threshold energy of the electron-induced double K -shell ionization of Al [36].

The parameters of the Campos [Eq. (15)] and Pattard-Rost [Eq. (16)] models were numerically optimized in a least-squares fit of the experimental cross-section integrals $\Pi_{TS}^{\text{expt}}[E_e^{(m)}]$ with Eq. (18). For the Campos model, only A_{TS} and B_{TS} could be used as free fitting parameters, whereas the threshold energy had to be kept fixed at the value obtained with the above described method [see Fig. 6(b)]. This is due to the fact that some experimental Π_{TS}^{expt} close to the threshold are negative so that the fit may converge for negative values of $\ln(U')$. If one uses in the fit the constraint that the experimental Π_{TS}^{expt} should be zero below the threshold, the fit simply pushes up the fitted value of the threshold. The Campos parameters A_{TS} and B_{TS} obtained from the fit are presented in the second row of Table III. For the Pattard-Rost model, all parameters could be fitted, the threshold energy included. Results are presented in the fifth row of Table III. A fit with the Pattard-Rost model was also performed with

TABLE III. Fitted values of the Campos and Pattard-Rost parameters used for the determination of the TS double ionization cross sections. A_{TS} and σ_M are expressed in kb and $E_{\text{TS}}^{\text{thr}}$ and E_M in keV and B_{TS} and χ_v^2 are dimensionless parameters.

Model	A_{TS}	B_{TS}	$E_{\text{TS}}^{\text{thr}}$	χ_v^2
Campos ^a	1.29(21)	-0.93(5)	4.88(11)	0.36
	σ_M	E_M	$E_{\text{TS}}^{\text{thr}}$	χ_v^2
Pattard-Rost ^a	1.07(9)	6.71(36)	4.88(11)	0.47
Pattard-Rost ^b	1.00(10)	7.12(75)	4.55(24)	0.29

^aIonization threshold fixed in the fit.

^bIonization threshold free in the fit.

a fixed threshold energy. The σ_M and E_M values obtained from this second fit (see fourth row of Table III) were found, however, to be consistent within the fitting errors with the results obtained from the three parameters fit. For the three fits, the reduced chi-squares χ_v^2 are quoted in the fifth column of the table. Note that for a good fit the reduced chi-square should be close to 1 and for a poor fit significantly bigger than 1. In our case, all χ_v^2 are smaller than 1 because of the large uncertainties characterizing the experimental cross section integrals. Thus, for the present results all three fits can be considered as good and a more stringent test of the fits would need more precise experimental data. The curves corresponding to the cross-section integrals fitted with the Campos and Pattard-Rost (threshold energy free) models are depicted in Fig. 6 where they are compared to the experimental values.

From Fig. 6 and Table III, it seems that the Pattard-Rost model fits better the experimental cross-section integrals than the Campos model. This is, however, not really surprising because the Campos model was developed for the calculation of single-ionization cross sections. It can be also noted that the threshold energy obtained from the three parameters Pattard-Rost fit is consistent within the combined error with the value obtained from the intersection of the regression lines corresponding to the experimental data points located in, respectively below, the fast-increase region. The experimental cross sections $\sigma_{\text{TS}}(E_{\text{av}})$ determined from Eq. (22) and the associated “average” energies E_{av} are presented in Table II. They are compared to the values derived from the Campos and Pattard-Rost models in Fig. 7. As shown, the experimental results are affected by rather large uncertainties. The latter are mainly due to the fact that the TS cross sections were determined from the differences of two cross-section integrals whose uncertainties are almost as big as their differences. Nevertheless, the curves derived from the Pattard-Rost model and, to a smaller extent, from the Campos one, reproduce satisfactorily the experimental data. It should be noted, however, that only smaller uncertainties and more experimental data points in the near-threshold region, where electron-electron interactions are expected to be most important, could permit a meaningful comparison of the two models and to probe electron-electron correlation effects. A simpler and more straightforward method to determine the dependence of the TS cross sections on the incoming electron energy would have consisted to use very thin targets, i.e., targets with

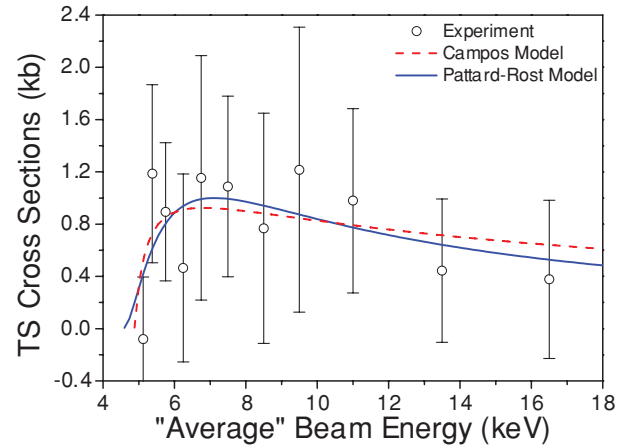


FIG. 7. (Color online) Electron-induced two-step double L_3M ionization cross sections σ_{TS} vs. the average value of the beam energy E_{av} in the first crossed target slice. The open circles represent the experimental values obtained with the slice division method described in the text, whereas the solid and dashed lines correspond to the theoretical two-step cross sections calculated using the Pattard-Rost [28,29] and Campos [14] models, respectively.

thicknesses in the order of $\mu\text{g}/\text{cm}^2$. In this case, the average energy of the incoming electrons is indeed almost equal to the nominal electron beam energy. However, due to the thinness of the target and the tiny values of the TS cross sections, the partial intensities of the $L\alpha M$ satellites corresponding to the TS process are then so small that they can no more be resolved from the background when the measurements are performed by means of high-resolution x-ray spectroscopy. In addition, due to the electron bombardment large amounts of heat are produced in the target. Test measurements performed with a $\sim 1\text{-}\mu\text{m}$ -thick Pd foil showed that the latter started to melt after a few minutes of bombardment. The target slice decomposition method employed in this work has thus permitted us to circumvent these intensity and heat load problems.

V. SUMMARY AND CONCLUDING REMARKS

The palladium $L\alpha$ x-ray spectrum induced by impact with medium-energy electrons was measured by means of high-resolution x-ray spectroscopy using a Bragg-type von Hamos bent crystal spectrometer. The measurements were performed for 15 different electron-beam energies ranging from 4 to 18 keV. From the observed intensity ratios of the resolved $L\alpha M$ satellites to the parent $L\alpha_{1,2}$ diagram lines the partial ratios corresponding to the TS process were determined as a function of the nominal electron energy, the contributions to the double L_3M ionization of the $L_1-L_3M_{4,5}$ CK transitions and shakeoff process having been subtracted beforehand. From the obtained partial intensity ratios the cross-section integrals associated to the TS process could be determined. It was found that the variation of the TS cross-section integrals as a function of the nominal electron energy can be well reproduced by using in their calculation the cross-section energy dependencies proposed by for the parametrization of $(e, 3e)$ collisions in mid- and high- Z elements. The parameters related to the two models were then determined by fitting the Campos, and Pattard and

Rost functions to the experimental TS cross-section integrals. By inserting the fitted parameters in the corresponding cross-section formulas of Campos and Pattard Rost, we were able to compute the variation of the TS cross section as a function of the electron energy. On the other hand, the experimental TS cross sections could be also determined directly from the measured cross-section integrals, using a model-independent method based on the decomposition of the thick target into slices. A very satisfactory agreement was observed between the model-dependent and pure experimental TS cross sections. Furthermore, in our opinion, the slice decomposition technique used in the present work could be very helpful in many charged particle-induced x-ray fluorescence measurements for which the fluorescence signal has to be determined as a function of the energy of the incoming particles and the use of a thick target is simultaneously mandatory to get a strong-enough signal.

ACKNOWLEDGMENT

The financial support of the Swiss National Science Foundation (Grant No. 200020-125124) is acknowledged.

APPENDIX A: CONTRIBUTION OF TRIPLY IONIZED STATES TO THE OBSERVED $L\alpha M$ SATELLITE YIELDS

According to MCDF calculations, some low-energy components pertaining to the second-order $L\alpha M^{(2)}$ satellite ($L_3M^{-2}-M_{4,5}M^{-2}$ transition) are partly overlapping with the first-order $L\alpha M$ satellite whose relative intensity was used to determine the two-step cross sections. The latter might be thus somewhat overestimated. $L_3^{-1}M^{-2}$ triple vacancy states may be created either directly via electron-induced L_3MM triple ionization or indirectly via electron-induced L_1M double ionization followed by $L_1-L_3M_{4,5}$ CK transitions. Note that the combination of L_2M double ionization followed by $L_2-L_3M_{4,5}$ CK transitions has not to be considered because for Pd $L_2-L_3M_{4,5}$ CK transitions are energetically forbidden. Furthermore, since in all measured $L\alpha$ spectra no structure could be observed in the energy region between 2862 and 2865 eV where, according to MCDF calculations, the most intense components of the second-order $L\alpha M^{(2)}$ satellite are expected, the contribution of the radiative decay of the $L_3^{-1}M^{-2}$ triple vacancy states to the observed $L\alpha M$ satellite yields was estimated theoretically.

The direct L_3MM triple ionization was assumed to be decomposable into a L_3M TS double ionization followed by an additional single M -shell ionization. The number of triply ionized Pd atoms N_{tri} produced per second is thus given by the number of atoms doubly ionized as a result of a TS process multiplied by the probability P_M for a single M -shell ionization, i.e.,

$$N_{\text{tri}} \approx N_{\text{TS}} P_M = N_{\text{TS}} n h_{\text{eff}} \sigma_M, \quad (\text{A1})$$

where n stands for the number of atoms per unit volume and h_{eff} the effective target thickness. Similarly, the TS process can be considered as a single L_3 -subshell ionization followed by a single M -shell ionization so

$$N_{\text{TS}} \approx N_{L_3} n h_{\text{eff}} \sigma_M, \quad (\text{A2})$$

and the N_{tri} to N_{TS} ratio can be approximated to:

$$\frac{N_{\text{tri}}}{N_{\text{TS}}}(E_e) \approx \frac{N_{\text{TS}}}{N_{L_3}}(E_e). \quad (\text{A3})$$

In the above relation the differences between the threshold energies corresponding to the single, double, and triple ionization were neglected. The relative excess of intensity of the $L\alpha M$ satellite due to the direct L_3MM triple ionization is then given by the following relation:

$$i_{\text{excess}}^{L_3MM}(E_e) \approx \frac{N_{\text{tri}}}{N_{\text{TS}}}(E_e) \frac{\sum I_{\text{MCDF}}^{\text{overlap}} \omega_{L\alpha M^2}}{\sum I_{\text{MCDF}}^{\text{tot}} \omega_{L\alpha M}}, \quad (\text{A4})$$

where $\sum I_{\text{MCDF}}^{\text{tot}}$ and $\sum I_{\text{MCDF}}^{\text{overlap}}$ represent the sum of the intensities of the MCDF components corresponding to the $L_3^{-1}M^{-2} \rightarrow L_3M^{-3}$ transition, respectively the sum of the intensities of the latter components which are overlapping with the $L_3^{-1}M^{-1} \rightarrow L_3M^{-2}$ transition and $\omega_{L\alpha M}$ and $\omega_{L\alpha M^2}$ stand for the partial fluorescence yields of the first- and second-order M -satellite lines. The fluorescence yields were determined with a statistical scaling procedure. From Eq. (A4) a maximum value of 1.8(2)% (at $E_e = 12$ keV) was found for the relative contribution of the direct triple ionization L_3MM to the TS DI cross sections listed in Table II.

As mentioned above, $L_3^{-1}M^{-2}$ triply ionized states may also be created indirectly via L_1M DI followed by $L_1-L_3M_{4,5}$ CK transitions. To probe the strength of the L_1M DI, the $L\beta_{3,4}$ x-ray lines ($L_1-M_{3,2}$ transitions) were measured. The spectrum was recorded at a beam energy of 16 keV. As the weak $L\beta_6$ x-ray line (L_3-N_1 transition) is lying on the high-energy tail of the $L\beta_3$ line [18] and because both lines are partly overlapping due to their large natural widths [37], only the $L\beta_4$ line was used to probe the L_1M DI. As shown in Fig. 8 no resolved line or asymmetry corresponding to the M satellite is visible

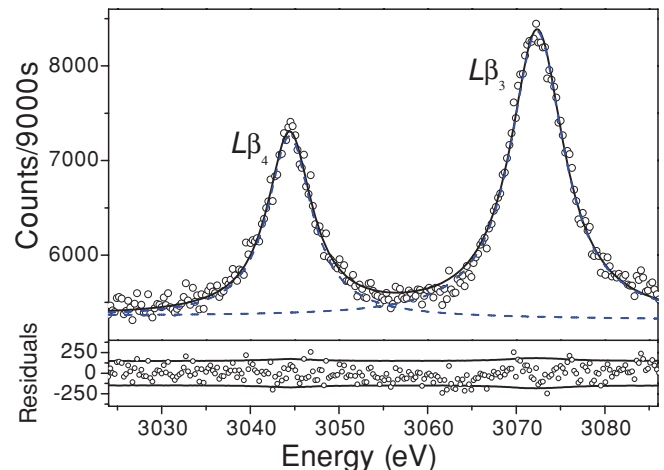


FIG. 8. (Color online) High-resolution $L\beta_{3,4}$ x-ray spectrum of Pd induced by impact with 16-keV electrons. The spectrum was fitted with two Lorentz functions. The thick solid line represents the total fit to the experimental data (open circles) and the dashed lines stand for the fitted $L\beta_4$ and $L\beta_3$ diagram lines. No satellite-induced asymmetry was observed in the high-energy tails of the diagram lines. Fit residuals are shown in the lower panel where they are compared with the statistical errors ($\pm 2\sigma$) of the data points (thin lines).

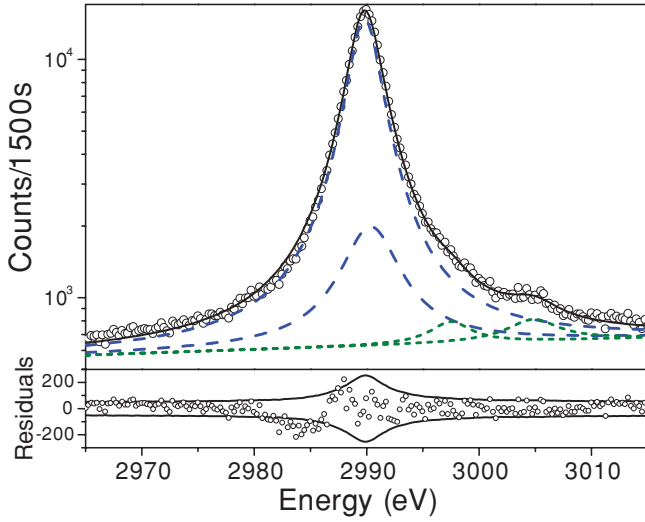


FIG. 9. (Color online) High-resolution $L\beta_1$ x-ray spectrum of Pd induced by impact with 15-keV electrons. The spectrum was fitted with four Lorentz functions. The thick solid line represents the total fit to the experimental data (open circles), the dashed lines the fitted $L\beta_1$ diagram line and $L\beta_1N$ satellite, and the dotted lines the $L\beta_1M$ satellites. Fit residuals are shown in the lower panel where they are compared with the statistical errors ($\pm 2\sigma$) of the data points (thin lines).

on the high-energy side of the $L\beta_4$ line, proving thus that the L_1M DI process is negligibly small.

A further contribution to the observed $L\alpha M$ satellite intensities may arise from L_2M DI followed by L_2-L_3N CK transitions. This sequence of processes leads indeed to $L_3^{-1}M^{-1}N^{-1}$ triple vacancy states whose radiative decay gives rise to x-ray transitions that are also overlapping with the $L\alpha M$ satellite. To probe the strength of the L_2M DI, the $L\beta_1$ x-ray line (L_2-M_4 transition) was measured at two different beam energies (10 and 15 keV). The spectrum measured at 15 keV is depicted in Fig. 9. As shown, M - and N -shell satellites are observed. The M satellites are mainly due to the electron-induced L_2M DI, whereas the N satellites arise from L_1-L_2N CK transitions. In the fit, the energy difference between the Lorentzians corresponding to the $L\beta_1N$ satellite

structure and $L\beta_1$ diagram line was kept fixed at the value provided by the MCDF calculations [19], whereas the widths and intensities of the two lines were let free. The $L\beta_1M$ satellite structure was fitted with two Lorentzians, whose widths, intensities, and centroid positions were used as free fitting parameters. From the fit a value of 2.8(6)% was found for the intensity ratio of the $L\beta_1M$ satellite to $L\beta_1$ diagram line. Similarly to Eq. (2), this ratio can be written:

$$i^*(E_e) = \frac{\omega_{L\beta_1M}}{\omega_{L\beta_1}} \frac{N_{\text{shake}}^*(E_e) + N_{\text{TS}}^*(E_e)}{(1 - f_{23})N_{L_2}(E_e) - N_{\text{shake}}^*(E_e) + f_{12}N_{L_1}(E_e)}, \quad (\text{A5})$$

where $\omega_{L\beta_1M}$ and $\omega_{L\beta_1}$ are the partial fluorescence yields of the $L\beta_1M$ and $L\beta_1$ transitions, respectively. The quantities N_s^* have the same meaning as in Eq. (2), the upper star indicating, however, that the shake and TS processes concern now the L_2 instead of L_3 subshell. Using similar calculations as those presented in Sec. III B, the two-step cross-section integrals $\Pi_{\text{TS}}^*(E_e)$ could be then derived. From the latter, the contribution $\Pi_{\text{TS}}^{\text{add}}$ of the L_2M DI followed by L_2-L_3N CK transitions to the experimental cross-section integrals $\Pi_{\text{TS}}^{\text{exp}}$ defined in Eq. (9) was determined, using the f_{23} CK rate quoted in Ref. [16]:

$$\Pi_{\text{TS}}^{\text{add}}(E_e) \approx f_{23}\Pi_{\text{TS}}^*(E_e). \quad (\text{A6})$$

Finally, $\Pi_{\text{TS}}^{\text{add}}:\Pi_{\text{TS}}^{\text{exp}}$ ratios of 1.3(7)% at $E_e = 15$ keV and 0.6(8)% at $E_e = 10$ keV were obtained.

In conclusion, the total contribution to the TS double ionization cross sections from processes leading to a triple ionization of the Pd atoms is 3.1(7)% for the highest beam energies (15 and 18 keV) and significantly smaller for energies below 10 keV. As the contribution varies with the beam energy, a systematic correction of the TS cross sections listed in Table II would have required to measure the $L\beta_{3,4}$ and $L\beta_1$ spectra at the 15 beam energies employed for the measurements of the $L\alpha$ spectra. However, since the corrections are rather small, we have renounced to perform these additional measurements and the systematic errors originating from the triple ionization were taken into consideration in the cross section uncertainties quoted in Table II.

- [1] T. Åberg, *Phys. Rev.* **156**, 35 (1967).
 [2] T. A. Carlson and M. O. Krause, *Phys. Rev.* **140**, 1057 (1965).
 [3] Y. V. Popov, C. Dal Cappello, B. Joulakian, and N. M. Kurmina, *J. Phys. B* **27**, 1599 (1994).
 [4] B. E. Marji, C. Schröter, A. Duguet, A. Lahmam-Bennani, M. Lecas, and L. Spielberger, *J. Phys. B* **30**, 3677 (1997).
 [5] J. Berakdar, A. Lahmam-Bennani, and C. Dal Cappello, *Phys. Rep.* **374**, 91 (2003), and references therein.
 [6] O. Mauron and J.-Cl. Dousse, *Phys. Rev. A* **66**, 042713 (2002).
 [7] C. J. Powell, *Rev. Mod. Phys.* **48**, 33 (1976).
 [8] E. J. McGuire, *Phys. Rev. A* **16**, 62 (1977).
 [9] M. Gryziński, *Phys. Rev.* **138**, A336 (1965).
 [10] C. S. Campos, M. A. Z. Vasconcellos, X. Llovet, and F. Salvat, *Phys. Rev. A* **66**, 012719 (2002).
 [11] K. Słabkowska and M. Polasik, *J. Phys. Conf. Ser.* **58**, 263 (2007).
 [12] M. Polasik, K. Koziol, K. Słabkowska, M. Czarnota, and M. Pajek, *J. Phys. Conf. Ser.* **163**, 012050 (2009).
 [13] S. Segui, M. Dingfelder, and F. Salvat, *Phys. Rev. A* **67**, 062710 (2003).
 [14] C. S. Campos, M. A. Z. Vasconcellos, J. C. Trincavelli, and S. Segui, *J. Phys. B* **40**, 3835 (2007).
 [15] D. V. Davis, V. D. Mistry, and C. A. Quarles, *Phys. Lett. A* **38**, 169 (1972).
 [16] W. Cao, J. Hozzowska, J.-Cl. Dousse, Y. Kayser, M. Kavčič, M. Žitnik, K. Bučar, A. Mihelič, J. Szlachetko, and K. Słabkowska, *Phys. Rev. A* **80**, 012512 (2009).
 [17] J. Hozzowska, J.-Cl. Dousse, J. Kern, and C. Rhême, *Nucl. Instrum. Methods B* **376**, 129 (1996).

- [18] R. D. Deslattes, E. G. Jr. Kessler, P. Indelicato, L. de Billy, E. Lindroth, and J. Anton, *Rev. Mod. Phys.* **75**, 35 (2003).
- [19] K. Słabkowska and M. Polasik, *Radiat. Phys. Chem.* **75**, 1471 (2006).
- [20] F. P. Larkins, *J. Phys. B: At. Mol.* **4**, 1 (1971).
- [21] S. L. Sorensen, S. J. Schaphorst, S. B. Whitfield, B. Crasemann, and R. Carr, *Phys. Rev. A* **44**, 350 (1991).
- [22] T. D. Thomas, *Phys. Rev. Lett.* **52**, 417 (1984).
- [23] P.-A. Raboud, M. Berset, J.-Cl. Dousse, Y.-P. Maillard, O. Mauron, J. Hozowska, M. Polasik, and J. Rzadkiewicz, *Phys. Rev. A* **65**, 062503 (2002).
- [24] T. Mukoyama and K. Taniguchi, *Phys. Rev. A* **36**, 693 (1987).
- [25] K. G. Dyall, *J. Phys. B* **16**, 3137 (1983).
- [26] [<http://physics.nist.gov/PhysRefData/Star/Text/contents.html>].
- [27] [<http://physics.nist.gov/PhysRefData/Star/Text/programs.html>].
- [28] J. M. Rost and T. Pattard, *Phys. Rev. A* **55**, R5 (1997).
- [29] T. Pattard and J. M. Rost, *Phys. Scr.*, T **80**, 295 (1999).
- [30] T. F. Coleman and Y. Li, *SIAM J. Optim.* **6**, 418 (1996).
- [31] M. Dingfelder, S. Segui, and J. M. Fernández-Varea, *Phys. Rev. A* **77**, 062710 (2008).
- [32] Z. An and Q. Hou, *Phys. Rev. A* **77**, 042702 (2008).
- [33] R. Diamant, S. Huotari, K. Hämäläinen, C. C. Kao, and M. Deutsch, *Phys. Rev. Lett.* **84**, 3278 (2000).
- [34] W. Cao, J.-Cl. Dousse, J. Hozowska, M. Žitnik, M. Kavčič, and K. Bučar, *Phys. Rev. A* **81**, 012501 (2010).
- [35] J. L. Campbell, *At. Data Nucl. Data Tables* **85**, 291 (2003).
- [36] K. Fennane, J.-Cl. Dousse, J. Hozowska, M. Berset, W. Cao, Y.-P. Maillard, J. Szlachetko, M. Szlachetko, and M. Kavčič, *Phys. Rev. A* **79**, 032708 (2009).
- [37] J. L. Campbell and T. Papp, *At. Data Nucl. Data Tables* **77**, 1 (2001).